

Cite this: DOI: 10.1039/c0xx00000x

www.rsc.org/xxxxxx

ARTICLE TYPE

Mechanical properties of electrochemically synthesised metal-organic framework thin films

Ben Van de Voorde^a, Rob Ameloot^a, Ivo Stassen^a, Maarten Everaert^a, Dirk De Vos^{a,*} and Jin-Chong Tan^{b,*}

⁵ Received (in XXX, XXX) Xth XXXXXXXXXX 20XX, Accepted Xth XXXXXXXXXX 20XX

DOI: 10.1039/b000000x

We investigate the mechanical properties of metal-organic framework thin-film coatings grown with an electrochemical method, which allows fast depositions in environmentally friendly solvents. For the first time Cu(CHDA) and Cu(INA)₂ are electrochemically synthesised as dense coatings on Cu-electrodes, alongside the well-known Cu₃(BTC)₂ (CHDA = *trans*-cyclohexane-1,4-dicarboxylate; INA = isonicotinate; BTC = benzene-1,3,5-tricarboxylate). In order to probe the mechanical behaviour of the MOF coatings, both nanoindentation and nanoscratch experiments are performed. The indentation of a polycrystalline film allows the determination of average Young's moduli and hardness of the coatings. Cu(CHDA) exhibits the highest stiffness and hardness, with values of 10.9 GPa and 0.46 GPa respectively. Intermediate values are obtained for the well-known Cu₃(BTC)₂ and the smallest values for Cu(INA)₂. A close inspection of the crystal lattice of the MOF materials under investigation, allows for correlating mechanical properties and structural building units of these materials. Finally, the effect of the fundamental mechanical properties of MOF films on their scratch and wear resistance is illustrated.

1 Introduction

Metal-organic frameworks (MOFs) are a hybrid class of crystalline materials, combining both inorganic and organic building blocks.¹ This offers an unique range of properties; such as framework flexibility^{2,3}, uniform pore sizes¹, easy functionalization⁴, high porosity⁵ and chemical stability^{6,7}. The synthesis of continuous, thin MOF films on solid substrates opened the door for applications in membranes⁸, sensors⁹ and low-κ dielectrics¹⁰. It is therefore not surprising that different synthesis methods have recently been developed for the preparation of MOF films.⁹ Strategies such as the solvothermal synthesis from a mother solution¹¹, layer-by-layer deposition¹², the use of stable precursor solutions¹³ or galvanic displacement¹⁴ have successfully been employed for thin film synthesis. A major disadvantage of many of these methods, remains the large amounts of waste that are generated during the synthesis, especially considering the used metal salts. In order to avoid large amounts of waste, the risks and costs associated with anions such as nitrates and chlorides, respectively oxidation and corrosion hazards, an electrochemical synthesis method was proposed.¹⁵ This method was pioneered for copper-based MOF materials (Cu₃(BTC)₂), but most recently a number of different metal electrodes (Al, Zn, Fe) were successfully used.^{16,17} The method is based on the dissolution of a metallic anode and subsequent release of metal ions into a solution containing the organic linker. By carefully modifying the synthesis conditions, films consisting of one-crystal thick layers can be synthesised. Notably the filling of gaps in the coating to

yield a continuous film seems to be an intrinsic property of electrochemical MOF growth, as exposed metal substrate serves as a building block reservoir rather than just as a possible anchoring point.¹⁸ Electrochemical synthesis offers also very short synthesis times, ranging from several seconds up to a few minutes in non-toxic solvents like ethanol and water.¹⁸ Given the recent research focus on the preparation of MOF films, it is remarkable how little is known about film mechanical behaviour or film-to-substrate adhesion strength, which are important aspects when considering practical applications. For example, in stress-induced chemical sensors, such as microcantilevers, film stiffness (Young's modulus) and film-to-substrate adhesion are key mechanical parameters that affect the attainable detection limit.¹⁹ Up till now, the mechanical properties of MOFs have only sparsely been investigated. However recent studies allow more insight into the elastic properties of these hybrid materials.^{20–24} The mechanical response of MOFs when subjected to loads below the material yield strength, leads to small reversible deformations or elastic strains. By using a nanoindenter this load-deformation relationship can be determined, allowing for the calculation of the corresponding elastic modulus (E) (or Young's modulus) and the hardness (H) of single crystals and films.²⁰ The values obtained from single crystals, show that MOFs and hybrid framework materials can exhibit dramatically different mechanical properties (especially E and H), spanning the range of organic polymers, ceramics and metallic materials.²⁰ However, most studies focus mainly on indentations of single crystals,^{23–25} only two studies have briefly touched on the

mechanical properties of MOF-films.^{10,24} Bundschuh *et al.*²⁴ performed an indentation study on the (100) plane of an epitaxially grown film of Cu₃(BTC)₂ to obtain the corresponding Young's moduli and hardness ($E_{(100)} = 9.3$ GPa and $H_{(100)} = 0.20$ GPa). The solvothermal method employed by Eslava *et al.*¹⁰ resulted in ZIF-8 films without preferential crystal facets on the film surface (i.e. textureless). In this case, E and H were obtained by assuming the presence of a randomly-oriented crystal facet on the film surface, resulting in an average value of Young's modulus and hardness to be measured *via* indentation experiment ($E = 3.5$ GPa and $H = 0.43$ GPa).

In this work, the mechanical properties of three different electrochemical Cu-MOF coatings have been investigated in detail. For the first time Cu(INA)₂ and Cu(CHDA), constructed from isonicotinic acid (INA)²⁶ and *trans*-1,4-cyclohexanedicarboxylic acid (CHDA)²⁷ respectively, were electrochemically synthesised as densely packed coatings. The coatings were subjected to nanoindentation measurements to determine the values of E and H. In addition, nanoscratch tests have been conducted for the first time on MOF-films. It should be noted that the resistance of a MOF-film to abrasion and scratching is of high importance considering the stresses and strains such coatings would have to sustain in real-life applications. Nano-scratching is already a well-known technique for characterising the wear resistance of materials such as ceramics, oxides, metals and organic polymers.^{28–32} Furthermore, nanoscratch experiments can provide insight into the attachment strength of the film to the substrate, by determining the applied force needed for delamination.³¹

2 Experimental

2.1 Electrochemical synthesis of MOF coatings

In 100 ml of solvent mixtures of EtOH : H₂O with different ratios, 5.8 mmol of ligand (1,3,5-benzenetricarboxylic acid, *trans*-1,4-cyclohexanedicarboxylic acid or isonicotinic acid) was dissolved and stirred until a clear solution was obtained. To this mixture 6.42 mmol of tributylmethylammonium methyl sulfate (MTBS) was added, which serves as a conduction salt during the electrochemical synthesis. The clear solution was heated to 328 K and pure copper electrodes (3 cm x 1 cm x 2 mm) spaced 1 cm apart were partially immersed in the solution. By applying a chosen voltage (1–30 V), MOF-films were grown on the anode under static conditions. After the required synthesis time (ranging from 1 to 180 s), the coatings were washed with ethanol to remove unreacted ligand and Cu²⁺ ions.

2.2 Characterization

Powder XRD patterns were recorded on a STOE STADI P Combi instrument in Debye Scherrer geometry (Cu K α 1) using an IP position-sensitive detector ($2\theta = 0–60^\circ$; $\Delta 2\theta = 0.03^\circ$). Film XRD patterns were recorded on a STOE STADI MP in Bragg–Brentano mode ($2\theta - \theta$ geometry; Cu K α 1) using a linear position-sensitive detector: step width 0.5° 2θ ($2\theta = 5–40^\circ$; $\Delta 2\theta = 0.01^\circ$). Scanning electron micrographs of MOF coatings on pure copper electrodes were recorded on either Au-coated samples using a Philips XL30 FEG microscope or on non-coated samples on a Carl Zeiss Evo LS15 environmental SEM.

2.3 Nanoindentation and nanoscratch experiments

Nanoindentation experiments were performed using an MTS Nanoindenter equipped with the DCM II head (Dynamic Contact Module II). Indentations were conducted under the displacement-controlled CSM mode (Continuous Stiffness Measurement), so that the values of E and H can be determined as a function of the surface penetration depth. A 2-nm sinusoidal displacement at 45 Hz was superimposed onto the system's primary loading signal, and the loading and unloading strain rates were set at $5 \times 10^{-2} \text{ s}^{-1}$. All tests were performed to a maximum indentation depth of 1000 nm using a Berkovich diamond tip. The raw data (load-displacement curves) obtained were analysed assuming a Poisson's ratio of 0.18 and by using the Oliver and Pharr method.³³ A typical load displacement curve is presented in Figure S1. The nanoscratch tests were performed on the MTS Nanoindenter using the XP head. During the scratch tests, the specimen with a coated surface was laterally translated under the indenter head while maintaining a prescribed load, for a total scratch length of 50–100 μm at a speed of 5 $\mu\text{m/s}$ in the 0° or 180° direction (Figure S2). During a ramp load scratch test (RLS) the normal load was progressively increased from 0 to 10–40 mN at a loading rate of 0.5 mN/s. The pass and return wear scratch test (PRW) has a constant load of 1 mN and each cycle consists of a pass in the 0° direction and a return in the 180° direction. For the PRW 10 cycles were performed. For each scratch test, a set of surface profiles along the track was measured, including the track profile before scratch (Profile), during scratch (Scratch) and after scratch (Post-profile). The profiling load was set at a relatively small value of 50 μN with a profiling velocity of 1 $\mu\text{m/s}$.

2.4 Evaluation of crystallinity

To evaluate the crystallinity under increased uniaxial pressure, a literature method was followed.³⁴ MOF powder was pressed between two metal blocks at pressures ranging from 0 to 250 bar. The pressure was kept for 30 seconds, after which an XRD diffractogram was taken. The broadening of the diffraction peaks at low angles $5–20^\circ$ 2θ is analysed using the full width half mid-height (FWHM) calculations in OriginPro 9.0 software.

3 Results

3.1 Synthesis of MOF coatings

As could be expected from the solvothermal synthesis conditions for Cu₃(BTC)₂, Cu(CHDA) and Cu(INA)₂, the rate of nucleation and growth is different for each MOF during electrochemical deposition.^{26,27,35} In order to make dense coatings, the influence of the synthesis conditions (voltage, time, ...) on the coverage and thickness of the films was investigated. Carefully controlling these parameters, together with the composition of the solvent (mixtures of EtOH:H₂O in different ratios), allowed the synthesis of dense coatings of the three MOFs (Figure 1 and S3). Due to different formation kinetics, the size of MOF crystallites constituting the three coatings is different. While Cu₃(BTC)₂ has crystals up to 15 μm , the crystal size of the highly intergrown Cu(CHDA) film is around 3 μm and Cu(INA)₂ coatings consist of intergrown crystals smaller than 2 μm . The thickness of the coatings was evaluated by cross-section SEM (Figures S4–6) and measured accordingly: Cu₃(BTC)₂ 11–15 μm , Cu(CHDA) 1.3–1.5

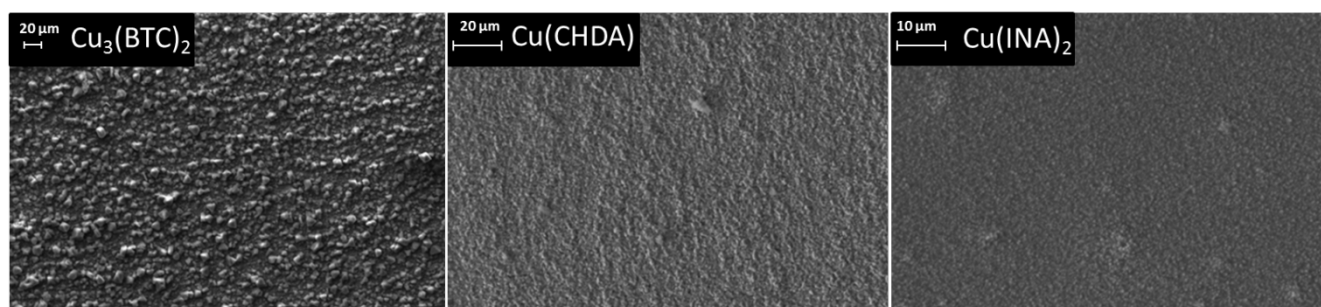


Figure 1. Electrochemical growth of $\text{Cu}_3(\text{BTC})_2$, $\text{Cu}(\text{CHDA})$ and $\text{Cu}(\text{INA})_2$ on copper anodes.

5 μm and $\text{Cu}(\text{INA})_2$ 1.6-1.9 μm . The synthesis conditions are summarised in table S1 in the supporting info.

3.2 Indentation experiments

The stiffness of a material under an elastic strain (reversible) is denoted as the elastic modulus (E), while the hardness (H) indicates the resistance of the material towards plastic deformation (irreversible).³⁶ These mechanical properties of a small volume of material are most frequently measured using indentation techniques, for which CSM is the ideal technique, especially for mechanical property measurements of thin films.³⁷ In a conventional nanoindenter, the contact stiffness can be inferred from the initial unloading contact stiffness, more specifically the slope of the initial portion of the unloading curve. When using the CSM technique, contact stiffness can be extracted continuously during the loading portion of the indentation test, by superimposing a harmonic oscillation onto the nominally increasing load (Figure S1). This makes the CSM technique ideal for thin films and graded materials, as the elastic modulus and hardness can be monitored as a function of indentation depth.³⁷ As the MOF films in this study consist of randomly oriented crystallites exposing different crystal facets, a large variation in load-displacement behaviour is to be expected (Figures S7-9), especially considering the anisotropy in mechanical properties in the MOF crystals and the grain boundary phenomena in the polycrystalline film.^{24,25,26,39} The largest variation in these load-displacement curves can be found for $\text{Cu}_3(\text{BTC})_2$, coinciding with the relatively large roughness of the $\text{Cu}_3(\text{BTC})_2$ coating. Nevertheless, these indentation experiments will give a good insight into the mechanical properties of the complete film, as the indenter tip is sufficiently large (Berkovich face angle $\sim 142^\circ$) to indent several crystallites per indent and each film is indented more than 15 times (increasing the number of indents did not change the standard deviation significantly). In Figure 2 representative load-displacement curves for the three MOF-films are shown. Distinct differences are clearly observed for the load-displacement curves of the three types of materials. The load developed during the indentation of the $\text{Cu}(\text{CHDA})$ film reaches a maximum magnitude of ~ 8 mN, while for $\text{Cu}_3(\text{BTC})_2$ and $\text{Cu}(\text{INA})_2$, the maximum loads are ~ 2 mN and ~ 1 mN respectively. An important property that can be derived directly from the load-displacement curves is the elastic recovery upon unloading,

where the vertical displacement recorded by the unloading curve is directly proportional to the elastic recovery of the materials. They are calculated at these applied maximum loads to be 40% for $\text{Cu}(\text{CHDA})$, 25% for $\text{Cu}_3(\text{BTC})_2$ and 14% for $\text{Cu}(\text{INA})_2$.

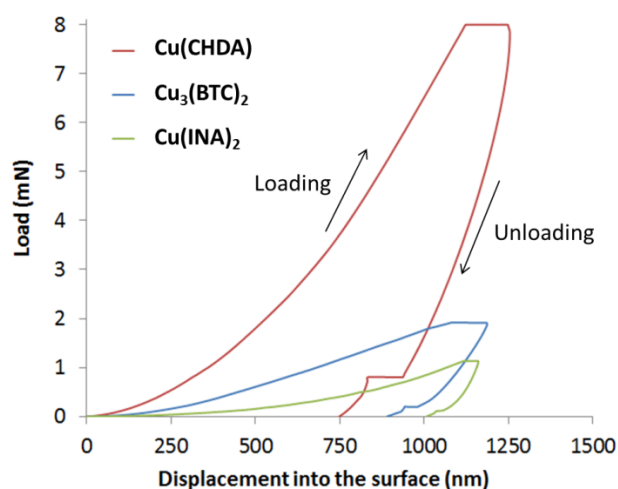


Figure 2. Typical load-displacement curves of $\text{Cu}_3(\text{BTC})_2$, $\text{Cu}(\text{CHDA})$ and $\text{Cu}(\text{INA})_2$ films.

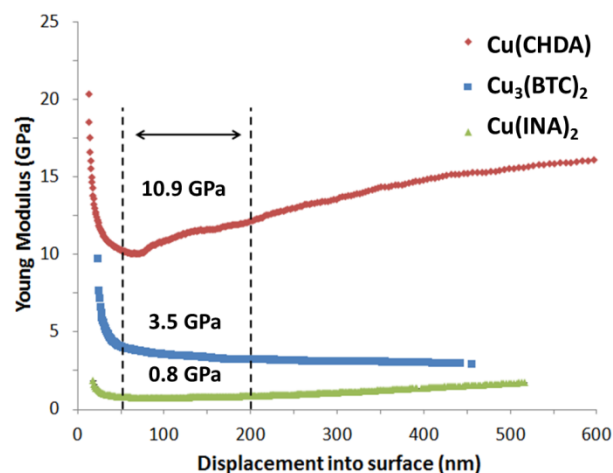


Figure 3. The average Young's moduli as a function of indentation depth, corresponding to the 15 individual indentations with standard deviations for $\text{Cu}(\text{CHDA})$, $\text{Cu}_3(\text{BTC})_2$ and $\text{Cu}(\text{INA})_2$ of 3.1, 2.5 and 0.3 GPa respectively.

Table 1. Young's modulus (E), hardness (H) and plasticity index (Ψ) of the MOF films (averaged over an indentation depth of 50-200 nm), together with the theoretical density and % solvent accessible volume (SAV corresponds to internal pore volume).

	E (GPa)	H (GPa)	Ψ^b	Density ^c	SAV(%) ^d
Cu(CHDA)	10.9 \pm 3.1	0.46 \pm 0.14	0.63	1.49	25
Cu₃(BTC)₂	3.5 \pm 2.5	0.17 \pm 0.16	0.79	1.22	50
Cu(INA)₂	0.8 \pm 0.3	0.02 \pm 0.01	0.86	1.51	22

^a The errors correspond to standard deviations on more than 15 measurements. ^b The plasticity index was calculated following a literature method.³⁰ ^c The theoretical framework densities as given in the cif files, with the units g/cm³. ^d Solvent Accessible Volume (in %) computed using the "VOID" algorithm implemented in the PLATON package.

Using the CSM load-displacement data, the E and H are calculated with the method of Oliver and Pharr.³³ Similar as with the load-displacement curves, the largest variation in the E and H as a function of indentation depth (Figures S10-15), can be found for Cu₃(BTC)₂, due to the surface roughness of the film. The average E and H as a function of indentation depth of 15 indents are presented in Figure 3 and 4. As the thickness of the MOF-coatings is only a few microns, a contribution of the Cu substrate is to be expected if the indentation is too deep. For Cu(CHDA) and Cu(INA)₂ the curves in Figure 3, representing E versus the displacement into the surface show an increase of E with indentation depth. This can be understood as a contribution of the underlying Cu substrate to the calculated moduli, which is absent when probing the relatively thick Cu₃(BTC)₂ coating. However, as the elastic modulus of the substrate (>50 GPa) is a factor of three times larger than the recorded values of the films, the effect of the substrate on the obtained values will be minimal. To minimise this effect, the range for the calculation of the E and H values was set from 50 to 200 nm indentation depth (Table 1).

As is clear from the nanoindentation results summarised in Table 1, substantial differences in E and H are observed for the three materials. It should be taken into account that the indentation data are collected for a polycrystalline film with different crystal orientations in which grain boundary phenomena may affect the indentation results. These considerations together with the roughness of the films are a direct explanation for the large standard deviations in mechanical properties (Table 1). Nevertheless, clear correlations can be made between the results for these different materials and their structural properties. Cu(CHDA) has the largest stiffness (E = 10.9 GPa) and hardness (H = 0.46 GPa) of the three materials. This high average stiffness and hardness can be related to the presence of rigid Cu-oxo chains running along the *c*-axis in the crystal lattice (Figure S16), leading to a relatively high crystal density of 1.49 g/cm³ (Table 1).

Compared to Cu(CHDA), the stiffness (E = 3.5 GPa) and hardness (0.17 GPa) of Cu₃(BTC)₂ are three times smaller. Here the E for the (randomly oriented) polycrystalline film is substantially lower compared to a previously obtained E in the study of Bundschuh *et al.* of an epitaxially grown Cu₃(BTC)₂ film (E = 9.3 GPa), in which only the (100) facets are indented such that no elastic anisotropic effects are taken into account. The hardness of the Cu₃(BTC)₂ film (H = 0.17 GPa) is however in

good agreement with the literature value (H = 0.2 GPa).²⁴ This observation suggests that less anisotropy in hardness is present, which is consistent with previously published studies.^{39,40} The material with both the smallest E and H is Cu(INA)₂, with 0.8 and 0.02 GPa respectively; these results are counterintuitive given that the density of the Cu(INA)₂ framework is indeed the

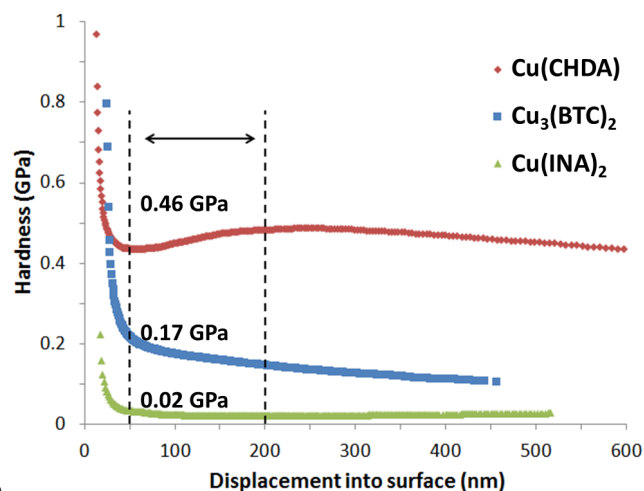


Figure 4. The average hardness as a function of displacement into the surface, corresponding to the 20 individual indentations with standard deviations (15 measurements) for Cu(CHDA), Cu₃(BTC)₂ and Cu(INA)₂ of 0.14, 0.16 and 0.01 GPa respectively.

highest of the three materials studied here (SAV% the lowest). Notably our previous work on a subfamily of MOFs (termed ZIFs) has established that the elastic modulus scales with framework density and SAV%.³⁶ The values we obtained here for Cu(INA)₂ are comparable with soft organic polymers, with E's ranging from 0.1 GPa up to 10 GPa and H's ranging from 0.01 GPa up to 0.4 GPa.²⁰ Such low values can be related to the physical properties and molecular structure of the framework. In particular it is known that Cu(INA)₂ can exhibit an expansion-contraction of up to 10 volume % of the framework (Figure S17).²⁶ Reversible expansions of the framework under stimuli like temperature, the presence of guest molecules or pressure are known as breathing behaviour.^{2,3} Because the atomic displacement can reach up to several Å, the mechanical response of the framework to an applied force is expected to be different from that of non-breathing frameworks, like Cu(CHDA) and Cu₃(BTC)₂. Recent theoretical studies have predicted that breathing can have a large effect on the mechanical properties, leading to very low E's and large anisotropies.³⁸ In light of this, our observations for Cu(INA)₂ support the idea that materials with pronounced breathing behaviour may exhibit relatively low value of E. Furthermore, the very low hardness could arise from the weaker Cu-nitrogen bond compared to the Cu-oxygen bond in the other frameworks, like Cu(CHDA) and Cu₃(BTC)₂. However, a detailed single-crystal Brillouin scattering study accompanied by density-functional computations are needed to establish the full set of Cu(INA)₂ elastic constants, from which the underlying deformation mechanisms can be elucidated (for example, see ref.[22]).

Additionally, in an attempt to quantify the relative plastic/elastic behaviour of the coatings, the plasticity index (Ψ) was calculated and presented in table 1.³⁰ Cu(INA)₂ has the highest plasticity





index, followed by $\text{Cu}_3(\text{BTC})_2$ and $\text{Cu}(\text{CHDA})$. The plasticity index of $\text{Cu}(\text{CHDA})$ (0.63) is comparable with organic polymer films like polymethylmethacrylate (0.6), polystyrene (0.58) and polycarbonate (0.58).⁴¹ While the high plasticity index of $\text{Cu}_3(\text{BTC})_2$ (0.79) and $\text{Cu}(\text{INA})_2$ (0.86) are comparable with metallic films, like stainless steel (0.89) and $\text{Al}_{12}(\text{Fe,Cr})_3\text{Si}_2$ (0.78).⁴² However, for $\text{Cu}(\text{INA})_2$ we propose that the high plasticity index observed here may be linked to the breathing behaviour of this open-framework material, rather than purely due to (irreversible) plastic response alone.³⁸ Moreover, it is clear from these results that, MOFs have plasticity indices spanning over organic and inorganic materials, making them a true hybrid class of materials.¹

3.3 Scratch experiments

In order to probe the cohesion and attachment strength of the films, nanoscratch experiments using a Berkovich indenter tip were performed. The three-faced pyramidal geometry of the indenter tip makes it possible to perform two different scratch movements (Figure S2), with either the sharp tip or blunt side facing the scratching direction, hereafter referred to as ploughing and pushing, respectively.

Ramp-load scratches. In the first set of scratch experiments, the applied force was linearly increased along the scratch distance, from 0 up to 10 mN. Representative scratch profiles in the ploughing mode and pushing mode are presented in Figures 5 and S6. During the scratch sequence a profile scan is performed in the direction of scratch length. The roughness of the $\text{Cu}_3(\text{BTC})_2$ coating is significantly larger compared to the other samples. The sharp peaks of the profiles indicate the edges of the different crystals. The roughness is therefore directly proportional with crystallite size, as can be seen in the profile scans of the coatings (Figures 5 and S18). The roughness after the scratch experiment was calculated for the three coatings and was independent of the scratch mode; $\text{Cu}_3(\text{BTC})_2$ had the highest roughness, followed by $\text{Cu}(\text{CHDA})$ and $\text{Cu}(\text{INA})_2$ (table 2).

Table 2 The average scratch depth at maximum load (10 mN) and the residual roughness^a.

	Scratch mode	$\text{Cu}(\text{CHDA})$	$\text{Cu}_3(\text{BTC})_2$	$\text{Cu}(\text{INA})_2$
Scratch depth		1380 ± 126	2720 ± 275	3280 ± 510
		1150 ± 133	1950 ± 71	1500 ± 424
Residual roughness		65 ± 4	105 ± 7	35 ± 1
		55 ± 1	107 ± 23	28 ± 10

^a The scratch depth and residual roughness is presented in nm averaged over three scratches together with the calculated standard deviation.

The depth at maximum applied load, i.e. at the end of the scratch, for the three materials are significantly different and can be related to the mechanical properties obtained in the indentation experiments. For the two scratch modes the results are presented in Table 2.

In ploughing mode, the material with the highest hardness, $\text{Cu}(\text{CHDA})$, is only penetrated up to 1380 ± 126 nm at 10 mN, while the very soft and flexible $\text{Cu}(\text{INA})_2$ is penetrated up to 3280 ± 510 nm. Notice that for $\text{Cu}(\text{CHDA})$ this penetration depth

is indeed smaller than the thickness of the coating, while for $\text{Cu}(\text{INA})_2$ the penetration depth is larger than the thickness of the coating, therefore exposing the underlying substrate, as evidenced in figure 6 in the form of coating delamination. $\text{Cu}_3(\text{BTC})_2$, which has an intermediate hardness, also has an intermediate penetration depth of 2720 ± 275 nm. For the experiments in pushing mode the trend is similar, but the scratch depth is significantly smaller. $\text{Cu}(\text{CHDA})$ is penetrated up to 1150 ± 133 nm, $\text{Cu}_3(\text{BTC})_2$ up to 1950 ± 71 nm and $\text{Cu}(\text{INA})_2$ up to 1500 ± 424 nm. The use of the sharp edge in the ploughing mode results clearly in a deeper penetration depth, compared to the pushing mode.

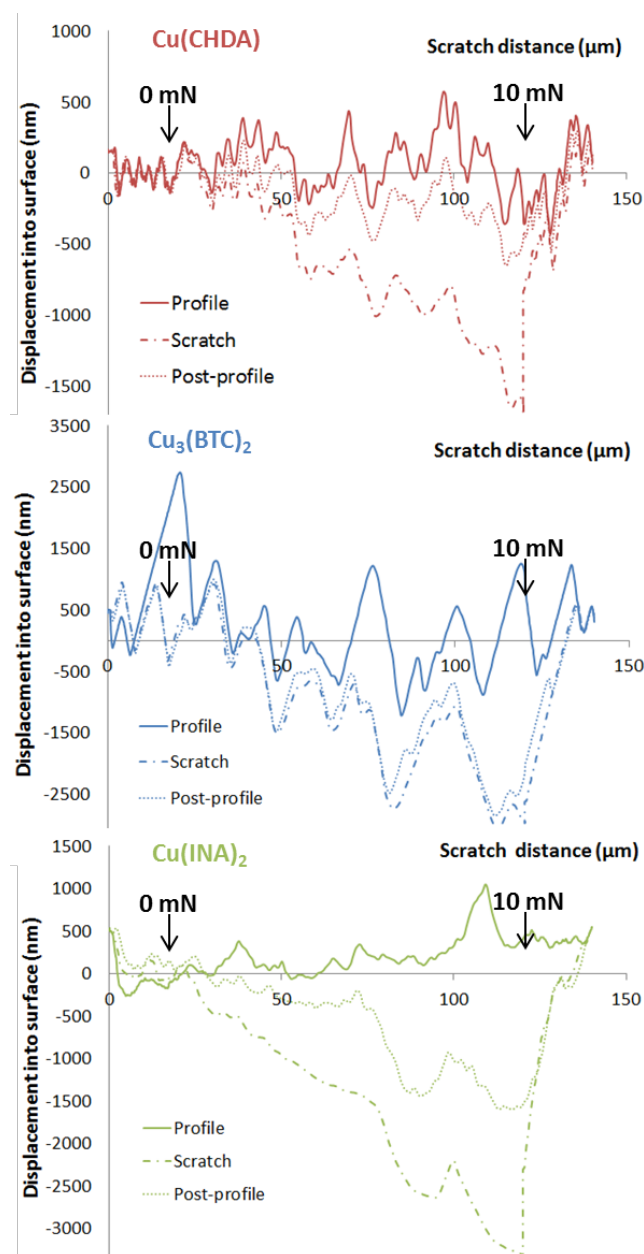


Figure 5. Scratch profiles in the plough mode with the displacement into the surface as a function of the scratch distance. The load was set at 0 mN at 20 μm and increased linearly up to 10 mN at 120 μm .

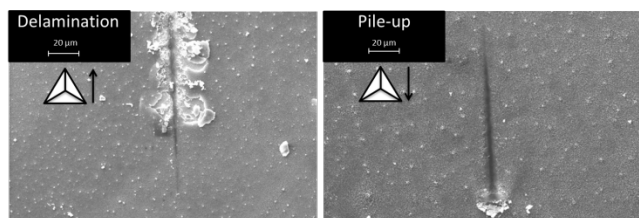


Figure 6. SEM pictures of scratches on the Cu(INA)₂ coating in the ploughing mode (left) and pushing mode (right).

Whilst it is well established that H is directly proportional to the resistance to scratch penetration,³⁰ further comparison of the scratch profile with the post-profile scan shows remarkable differences in elastic recovery of the materials. Here, the elastic recovery is defined as the difference in scratch depth and the post-profile scan, compared to the original profile scan. For Cu₃(BTC)₂ very little elastic recovery is detected, as the profile depth during the scratch and post-profile scan are very close to each other, reaching a maximum recovery of 200 nm or less than 10% of the scratch depth. For Cu(CHDA) and Cu(INA)₂ large elastic recoveries of more than 65% and 40% respectively are measured. So even though the scratch depth in the ploughing mode for Cu(CHDA) is more than 1300 nm (elastic deformation), the residual profile is only 400 nm deep (plastic deformation). The elastic recovery of Cu(CHDA) is comparable with that of organic polymers and nanocomposites (60-80%)^{43,44}, while Cu(INA)₂ has a similar value as a scratched zeolite MFI film (37%).⁴⁵ In order to further analyse the possible loss of mechanical integrity of the MOF films, scratches were evaluated by SEM. By studying the formation of pile-ups, cracks and possible delamination more insight into the plastic deformation can be gained.³⁰ Furthermore the effect of the scratch mode is clearly visible in Figure 6 for Cu(INA)₂. Delamination occurs in the ploughing mode after 40 µm (corresponding to 4 mN applied normal force), exposing the underlying Cu-electrode (substrate). The sharp edge of the indenter tip ploughs through the coating, dislodging coating fragments up to 25 µm from the scratch (Figure 6). The delamination suggests a poor bonding of the particles in the coating. On the contrary, when the indenter tip is set in the push mode, no delamination of the Cu(INA)₂ (Figure 6), or Cu(CHDA) and Cu₃(BTC)₂ coatings is observed. However, a clear pile-up is detected at the end of the scratch.

Wear-track scratches. To evaluate the abrasion resistance of the coating, a scratch wear test is performed with a constant applied load for ten cycles, for which each wear cycle consists of a scratch in both the ploughing mode and pushing mode. In order to evaluate the performance of the films, the wear track deformation is calculated as the area between the original surface profile and the tenth cycle's displacement into the surface, and is presented in Table 3 for the three materials with constant loads of 1 and 5 mN over a 50 µm wear distance. By increasing the load from 1 to 5 mN, the wear track deformation for all the coatings increases. This is to be expected considering the greater penetration depth that can be reached at increased applied load. For Cu(CHDA) and Cu₃(BTC)₂ the wear track deformation doubles; for Cu(INA)₂ a threefold increase is detected. Again the same trends can be observed as for the scratch experiments: the film of Cu(CHDA)

with the highest E and H has the smallest wear track deformation. Intermediate deformations are detected for Cu(INA)₂, while significantly larger deformations are registered for Cu₃(BTC)₂. In order to understand this very large wear track deformation the accompanying SEM pictures are presented in Figure 7, to elucidate the mechanisms taking place during the wear test. It can be seen that the large crystal size of Cu₃(BTC)₂ is an important factor contributing to the large wear track deformations.

Table 3 Wear track deformation^a at constant load of 1 or 5 mN over a wear distance of 50 µm.

	Cu(CHDA)	Cu ₃ (BTC) ₂	Cu(INA) ₂
1 mN	20 ± 9	105 ± 33	29 ± 4
5 mN	42 ± 2	213 ± 13	96 ± 1

^a The wear track deformation is presented as µm² ± standard deviation.

Similar as with the scratch tests, the very large Cu₃(BTC)₂ crystals are easily fractured and removed from the surface in subsequent runs, thus leading to very large wear track deformations. As can be seen in Figure 7, for Cu₃(BTC)₂ clear debris can be detected in the middle and at the end of the wear track, even resulting in an exposed Cu surface at a 5 mN applied force. Cu(CHDA) has almost no residual imprint after the wear test at 1 mN and no detached particles can be detected. Increasing the applied load to 5 mN leads to a clear visual wear track, but only very little debris can be seen at the end of the scratch. The very soft material Cu(INA)₂ has some debris for the 1 mN wear track and very clear delamination at the 5 mN wear track. This confirms that the delamination of the Cu(INA)₂ coating indeed occurs at an applied force between 1 and 5 mN, as seen in the ramp-load scratches (Figure 6).

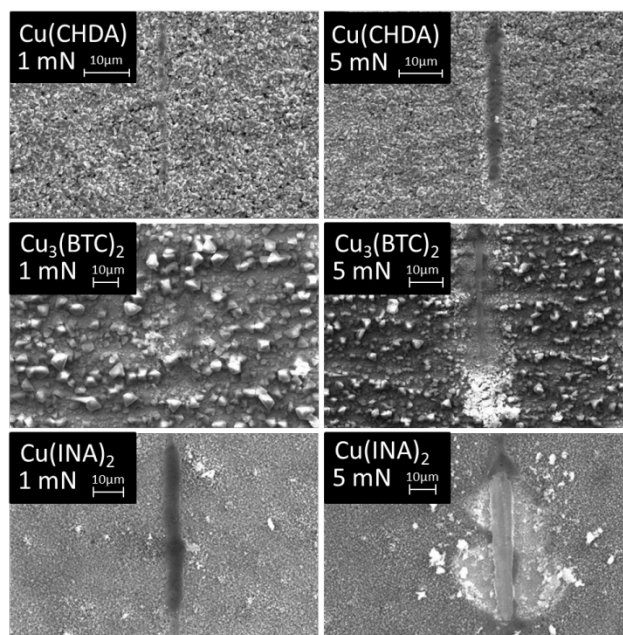


Figure 7. SEM pictures of the wear track scratch tests on the three MOF-films, comparing a 1 mN load with a 5 mN load.

4 Discussion

The indentation and scratch data show a clear correlation between

the structural characteristics and the mechanical properties. The material with the highest E and H values, Cu(CHDA), showed excellent scratch and wear resistance amongst the MOFs being interrogated here. The material with intermediate hardness and stiffness, Cu₃(BTC)₂, proved in the scratch experiments to be the least resistant to abrasion (Table 3) and displayed the largest plastic deformation (Figure 5, Post-profile). In order to understand this difference, the size of the crystals has to be considered. For Cu₃(BTC)₂, the large crystals lying in the scratch or wear path are fractured more easily as evident from SEM; some of these are subsequently being pulled out from the substrate leaving behind deep depressions which resemble plastic deformation (comparing scans after recovery in Figure 5). In contrast, the much smaller crystals of Cu(CHDA) and Cu(INA)₂ are being crushed under the tip, if there is no delamination, and are then compacted evenly forming a lubricant-like protective layer preventing further scarring of substrate surface (Figure 7 and Figure S19). Once the normal load is removed large elastic recovery is observed (Figure 5). Looking more closely at the SEM images of the scratch tests reveals a clear crushing of the crystals under compressive loading, rather than detachment (crystal pull-out) from the substrate surface. Even if the applied force is increased up to 40 mN, no delamination and only very little pile-up in the push mode is observed (Figure S19).

In future applications the structural integrity of the crystals after being subjected to external mechanical stresses is of paramount importance if the performance of the coatings is to be maintained. Therefore we have also evaluated the crystallinity of the three MOFs as a function of applied force, the results of which are presented in Figure 8 with corresponding SEM micrographs taken before and after the maximum pressure treatment shown in Figure S20.

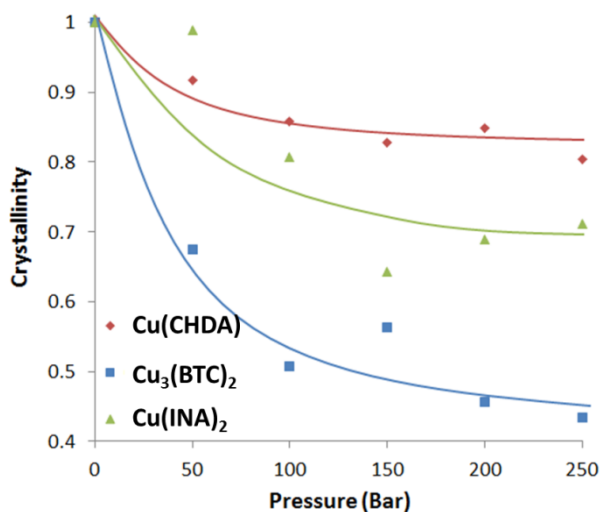


Figure 8. The crystallinity as a function of applied pressure. The lines are guides to the eye.

Again, Cu(CHDA) is structurally the most stable material, maintaining more than 80% of its crystallinity after a compression up to 250 bar. The SEM images show that the crystals of Cu(CHDA) are compressed into spherical aggregates of 10 µm. Even though the applied force is of a unilateral nature, the clusters of particles are densified into well-defined spherical

aggregates. The exact mechanism leading to formation of these spherical aggregates is not yet clear, but further experiments are conducted to unravel this peculiar behaviour of Cu(CHDA).

It is intriguing to see that the flexible material Cu(INA)₂ preserves up to 70% of its crystallinity, despite its relatively low E and H values obtained by nanoindentation. Nevertheless, a fragmentation of the freshly synthesised cubic crystals is observed after pressurisation at 250 bar (Figure S20). The observed compression of the crystals at low scratch loads combined with the results in Figure 8, indicate that at low load the crystallinity of the crystals is well preserved. The strong cohesion between the crystals does not result in a fragmentation of the crystals in the coating but results in a compression. However if the applied force reaches a threshold value of ~4 mN, delamination of the coating is observed, suggesting that the cohesion between the crystals is stronger than the attachment strength to the surface. The low hardness and weak interaction with the Cu-surface could be due to the weaker Cu-nitrogen bond, as compared to the Cu-oxygen bonds in Cu₃(BTC)₂ and Cu(CHDA).

Finally, Cu₃(BTC)₂ loses more than 50% of its original crystallinity, coinciding with a complete loss of octahedral crystal morphology in Figure S20. This is in good agreement with previous studies, where the pelletisation of Cu₃(BTC)₂ into tablets resulted in a loss of adsorption capacity due to the high pressure treatment during the shaping process.^{46,47} Thus Cu₃(BTC)₂ shows a dramatic loss of crystallinity at high pressures, combined with a poor substrate attachment strength in the scratch experiments. Although no significant detachment, but rather crushing of the crystals was detected for the ramp load scratch, during the wear test even at low loads (1 mN) debris is detected at the both sides and at the end of the scratch.

5 Conclusions

Carefully controlling the synthesis conditions allowed the fabrication of electrochemically grown MOF coatings of Cu(CHDA), Cu(INA)₂ and Cu₃(BTC)₂. Furthermore, the use of nanoindentation and nanoscratch experiments proved to be an excellent combination for establishing an improved understanding of the mechanical properties of thin-film MOF coatings. While indentation has enabled the determination of elastic moduli and hardness properties, the scratch experiments have enabled us to further characterise the abrasion resistance and provide insights into the differential adhesion strength of the coatings. Cu(CHDA) proved to be the stiffest and hardest tested material, with high elastic recoveries and abrasion resistance, indicating a strong substrate attachment strength. Moreover, these properties could be linked to the structural properties of the MOF framework itself, namely the rigid Cu-oxo chain running along the c-axis of the crystal lattice. Additionally, we have attributed the exceedingly low Young's modulus of Cu(INA)₂ to the flexible nature of its framework with breathing behaviour, while its low hardness is due to the weaker coordination bonding of the pyridine ring, which are anticipated to be more susceptible to bond breakage compared with stronger ionic and covalent bonding.

Acknowledgements

D.D.V. is grateful to KULeuven for support in the Methusalem grant CASAS, to IAP 7/05 (Belgium), to IWT (MOFShape) and FWO (K201513N and research projects). We wish to thank Professor Steve Roberts and Dr David Armstrong in the Department of Materials at Oxford University for giving us access to the nanoindenters.

Notes and references

^a Centre for Surface Chemistry and Catalysis (COK), KU Leuven,

10 Arenbergpark 23, B-3001 Leuven, Belgium. Fax: +32 16 32 19 98; Tel: +32 16 32 16 10; E-mail: dirk.devos@biw.kuleuven.be

^b Department of Engineering Science, University of Oxford, Parks Road, OX1 3PJ, Oxford, United Kingdom. Fax: +44 (0)1865 273906; Tel: +44 (0)1865 273925; E-mail: jin-chong.tan@eng.ox.ac.uk

15 † Electronic Supplementary Information (ESI) available: [Additional Figures s1-7, thin film and powder XRD diffractograms (Figures 8-13)]. See DOI: 10.1039/b000000x/

1. L. R. MacGillivray, *Metal-Organic Frameworks: Design and Application*, Wiley, 2010.
2. T. Loiseau, C. Serre, C. Huguenard, G. Fink, F. Taulelle, M. Henry, T. Bataille, and G. Férey, *Chemistry (Weinheim an der Bergstrasse, Germany)*, 2004, **10**, 1373–82.
3. B. Van de Voorde, A. Munn, N. Guillo, F. MILLANGE, D. E. De Vos, and R. I. Walton, *Physical Chemistry Chemical Physics*, 2013, **15**, 8606–8615.
4. B. Kesanli and W. Lin, *Coordination Chemistry Reviews*, 2003, **246**, 305–326.
5. B. Chen, M. Eddaoudi, T. M. Reineke, J. W. Kampf, and O. M. Yaghi, *Journal of the American Chemical Society*, 2000, **122**, 11559–11560.
6. K. S. Park, Z. Ni, A. P. Côté, J. Y. Choi, R. Huang, F. J. Uribe-Romo, H. K. Chae, M. O’Keeffe, and O. M. Yaghi, *Proceedings of the National Academy of Sciences of the United States of America*, 2006, **103**, 10186–91.
7. V. Guillermin, F. Ragon, M. Dan-Hardi, T. Devic, M. Vishnuvarthan, B. Campo, a Vimont, G. Clet, Q. Yang, G. Maurin, G. Férey, a Vittadini, S. Gross, and C. Serre, *Angewandte Chemie (International ed. in English)*, 2012, **51**, 9267–71.
8. H. Bux, C. Chmelik, R. Krishna, and J. Caro, *Journal of Membrane Science*, 2011, **369**, 284–289.
9. O. Shekhah, J. Liu, R. a Fischer, and C. Wöll, *Chemical Society reviews*, 2011, **40**, 1081–106.
10. S. Eslava, L. Zhang, S. Esconjauregui, J. Yang, K. Vanstreels, M. R. Baklanov, and E. Saiz, *Chemistry of Materials*, 2013, **25**, 27–33.
11. S. Hermes, F. Schröder, R. Chelmoski, C. Wöll, and R. a Fischer, *Journal of the American Chemical Society*, 2005, **127**, 13744–5.

12. O. Shekhah, H. Wang, S. Kowarik, F. Schreiber, M. Paulus, M. Tolan, C. Sternemann, F. Evers, D. Zacher, R. a Fischer, and C. Wöll, *Journal of the American Chemical Society*, 2007, **129**, 15118–9.
13. R. Ameloot, E. Gobechiya, H. Uji-i, J. a Martens, J. Hofkens, L. Alaerts, B. F. Sels, and D. E. De Vos, *Advanced Materials*, 2010, **22**, 2685–8.
14. R. Ameloot, L. Pandey, M. Van der Auweraer, L. Alaerts, B. F. Sels, and D. E. De Vos, *Chemical communications (Cambridge, England)*, 2010, **46**, 3735–7.
15. U. Mueller, H. Puetter, M. Hesse, and H. Wessel, 2005, WO 2005/049892A1.
16. A. M. Joaristi, J. Juan-alcan, P. Serra-crespo, F. Kapteijn, and J. Gascon, *Crystal Growth & Design*, 2012, **12**, 3489–3498.
17. N. Campagnol, T. Van Assche, T. Boudewijns, J. Denayer, K. Binnemans, D. De Vos, and J. Fransaer, *Journal of Materials Chemistry A*, 2013, **1**, 5827.
18. R. Ameloot, L. Stappers, J. Fransaer, L. Alaerts, B. F. Sels, and D. E. De Vos, *Chemistry of Materials*, 2009, **21**, 2580–2582.
19. A. Venkatasubramanian, J.-H. Lee, V. Stavila, A. Robinson, M. D. Allendorf, and P. J. Hesketh, *Sensors and Actuators B: Chemical*, 2012, **168**, 256–262.
20. J. C. Tan and A. K. Cheetham, *Chemical Society reviews*, 2011, **40**, 1059–80.
21. J.-C. Tan, P. J. Saines, E. G. Bithell, and A. K. Cheetham, *ACS nano*, 2012, **6**, 615–21.
22. J.-C. Tan, B. Civalieri, C.-C. Lin, L. Valenzano, R. Galvelis, P.-F. Chen, T. D. Bennett, C. Mellot-Draznieks, C. M. Zicovich-Wilson, and A. K. Cheetham, *Physical Review Letters*, 2012, **108**, 095502.
23. T. D. Bennett, J.-C. Tan, S. a Moggach, R. Galvelis, C. Mellot-Draznieks, B. a Reisner, a Thirumurugan, D. R. Allan, and A. K. Cheetham, *Chemistry (Weinheim an der Bergstrasse, Germany)*, 2010, **16**, 10684–90.
24. S. Bundschuh, O. Kraft, H. K. Arslan, H. Gliemann, P. G. Weidler, and C. Wöll, *Applied Physics Letters*, 2012, **101**, 101910.
25. D. Bahr, J. Reid, W. Mook, C. Bauer, R. Stumpf, a. Skulan, N. Moody, B. Simmons, M. Shindel, and M. Allendorf, *Physical Review B*, 2007, **76**, 184106.
26. J. Y. Lu and A. M. Babb, *Chemical Communications*, 2002, 1340–1341.
27. H. Kumagai, M. Akita-tanaka, K. Inoue, K. Takahashi, R. Loess, L. D. C. De Coordination, L. Pasteur, I. Le Bel, B. Pascal, and S. Cedex, *Inorganic chemistry*, 2007, **46**, 5949–5956.
28. J. L. Hay, R. L. White, B. N. Lucas, and W. C. Oliver, *Mat. Res. Soc. Symp.*, 1998, **505**, 325–330.

29. R. D. . Misra, R. Hadal, and S. . Duncan, *Acta Materialia*, 2004, **52**, 4363–4376. 45 47. M. G. Plaza, A. M. Ribeiro, A. Ferreira, J. C. Santos, U.-H. Lee, J.-S. Chang, J. M. Loureiro, and A. E. Rodrigues, *Separation and Purification Technology*, 2012, **90**, 109–119.
30. H. Yahyaei and M. Mohseni, *Tribology International*, 2013, **57**, 147–155.
31. F. Mammeri, E. Le Bourhis, L. Rozes, and C. Sanchez, *Journal of the European Ceramic Society*, 2006, **26**, 259–266.
32. E. Frutos, A. Cuevas, J. L. Gonzalez-carrasco, and F. Martin, *journal of the mechanical behavior of biomedical materials*, 2012, **16**, 1–8.
33. W. C. Oliver and G. M. Pharr, *Journal of Materials Research*, 2003, **19**, 3–20.
34. V. Guillermin, F. Ragon, M. Dan-hardi, T. Devic, M. Vishnuvarthan, B. Campo, M. Daturi, G. Clet, Q. Yang, G. Maurin, G. Férey, A. Vittadini, S. Gross, and C. Serre, *Angewandte Chemie (International ed. in English)*, 2012, **51**, 9267–9271.
35. S. S. Chui, S. M. Lo, J. P. H. Charmant, A. G. Orpen, and I. D. Williams, *Science*, 1999, **283**, 1148–1150.
36. J. C. Tan, T. D. Bennett, and A. K. Cheetham, *PNAS*, 2010, **107**, 9938–9943.
37. X. Li and B. Bhushan, *Materials Characterization*, 2002, **48**, 11–36.
38. A. U. Ortiz, A. Boutin, A. H. Fuchs, and F.-X. Coudert, *Physical Review Letters*, 2012, **109**, 195502.
39. W. Li, M. S. R. N. Kiran, J. L. Manson, J. a Schlueter, A. Thirumurugan, U. Ramamurty, and A. K. Cheetham, *Chemical communications (Cambridge, England)*, 2013, **49**, 4471.
40. J. C. Tan, J. D. Furman, and A. K. Cheetham, *Journal of the American Chemical Society*, 2009, **131**, 14252–14254.
41. J. B. Briscoe, L. Fiori, and E. Pelillo, *J. Phys. D: Appl. Phys.*, 1998, **31**, 2395–2405.
42. E. Frutos, A. Cuevas, J. L. Gonzalez-carrasco, and F. Martin, *journal of the mechanical behavior of biomedical materials*, 2012, **16**, 1–8.
43. A. Chafidz, I. Ali, M. E. A. Mohsin, R. Elleithy, and S. Al-Zahrani, *Journal of Polymer Research*, 2012, **19**, 9906.
44. H. Yari, S. Moradian, N. Tahmasebi, and M. Arefmanesh, *Tribology Letters*, 2012, **46**, 123–130.
45. N. Lauridant, T. J. Daou, G. Arnold, H. Nouali, J. Patarin, and D. Faye, *Microporous and Mesoporous Materials*, 2013, **172**, 36–43.
46. M. G. Plaza, A. F. P. Ferreira, J. C. Santos, A. M. Ribeiro, U. Müller, N. Trukhan, J. M. Loureiro, and A. E. Rodrigues, *Microporous and Mesoporous Materials*, 2012, **157**, 101–111.